

## **Prestack depth migration in anisotropic media by symmetric nonstationary phase shift**

Robert J. Ferguson and Gary F. Margrave

### **ABSTRACT**

A new depth imaging method for dipping transversely isotropic (TI) media is presented that is based on the symmetric nonstationary phase shift (SNPS) method of Ferguson and Margrave (1999). Their method is a cascade of two nonstationary extrapolators and is more accurate and more stable than other explicit-one-way extrapolators (Margrave and Ferguson, 1999b). Here it is adapted for depth imaging in a TI medium with no restriction placed on the degree of the anisotropy, its heterogeneity or its axis of symmetry. Depth imaging of two TI models (physical seismic data) by SNPS provides superior images to those from isotropic vertical transverse isotropy (VTI) methods.

### **INTRODUCTION**

Presently, much effort is spent on estimating the elastic parameters (P- and S-wave velocities) of an assumed isotropic subsurface for the construction of seismic images. Thomsen (1986) points out the inconsistency of these efforts when the subsurface is potentially anisotropic. Martin et al. (1992) demonstrate that isotropic algorithms applied to physical modeling data in transversely isotropic (TI) media produce mispositioning of plane reflectors and steep structures. Isaac and Lawton (1997) show that a TI medium having a symmetry axis of 45 degrees (measured from vertical) causes large errors in the lateral position of a simulated reef edge; enough error that an exploratory well would be significantly mispositioned.

Authors that have presented depth-imaging methods for TI media include Meadows et al. (1987) who extend the imaging method of Stolt (1978) to homogeneous media with elliptical anisotropy. Uren et al. (1990) present a 2-D poststack Stolt method for homogeneous TI, and Gonzalez et al. (1991) use an approximate anelliptic dispersion relation to implement a prestack Stolt method for P-waves in a homogeneous TI medium. Sena and Toksoz (1993) present a 2-D Kirchhoff algorithm (prestack) for weak TI (Thomsen, 1986). Uzcategui (1995) uses explicit depth extrapolators for TI media having a vertical axis of symmetry. Meadows and Abriel (1994), present a 3-D poststack phase-shift time algorithm for a homogeneous TI media to improve the image of data from the Gulf of Mexico. Kitchenside (1992) proposes a 2-D algorithm for homogeneous TI media that builds an extrapolator in the Fourier domain  $(k_x, \omega)$  and applies it as a truncated and tapered filter in the space-frequency  $(x, \omega)$  domain.

All of the above approaches restrict TI in the medium by assuming homogeneity (Meadows and Abriel, 1994; Kitchenside, 1992; Gonzalez et al., 1991), elliptical TI (Meadows et al., 1997), weak TI (Sena and Toksoz, 1993) or TI with a vertical axis of

symmetry (Uzcategui, 1995). No such restrictions are required for the depth imaging method presented here.

We borrow from Kitchenside (1992) in the initial development of the TI algorithm, but rather than applying a truncated filter in  $(x, \omega)$  we apply the complete filter in  $(k_x, \omega)$ . The resulting homogeneous phase-shift allows variation of velocity in the Fourier coordinates  $(k_x, \omega)$  and depth  $z$ . Generalization to heterogeneous TI is achieved using nonstationary filters. Implementation as a depth-imaging algorithm is done using the symmetric nonstationary filter approach of Ferguson and Margrave (1999a, 1999).

A difficulty in imaging TI media is discussed by Tsvankin (1997). For a TI medium with a dipping axis of TI symmetry, some phases of the propagating wavefield travel upwards. Our implementation is a process analogous to the turning wave migration of Hale et al. (1992). Down going phases are isolated and propagated down, and the upgoing phases are propagated up. The combination of the resulting spectra approximates the exact result, with error due to extrapolating the upgoing phases with a portion of the downgoing phases.

Two examples of depth imaging by SNPS in TI media are presented. The SNPS images are compared to isotropic depth imaging and a method that assumes a vertical axis of TI symmetry, and demonstrate the utility of SNPS, and its superiority over the other two imaging methods.

## REVIEW OF TRANSVERSE ISOTROPY

Transverse isotropy is a material symmetry that allows a complete specification of the elastic properties of the material with five constants. In this section, the phase velocity of P-waves in TI media is derived from first principles. It is a collection of the work of a number of authors, and is intended as a convenient reference. The derivation begins with the most general stress-strain relationship, having 81 elastic constants, and ends with the Thomsen (1986) phase velocity for P-waves.

The most general linear relationship between applied stress  $\sigma$  and material strain  $\epsilon$  requires nine stresses  $\sigma_{ij}$ , 9 strains  $\epsilon_{ij}$ , and 81 elastic constants  $c_{ijkl}$ . Using the summation convention of repeated indices

$$\sigma_{ij} = c_{ijkl} \epsilon_{kl} \quad (1)$$

where indices  $(i, j, k, l)$  take on values of 1, 2, and 3. The symmetry of stresses  $\sigma_{ij} = \sigma_{ji}$ , and strains  $\epsilon_{ij} = \epsilon_{ji}$  reduce the numbers of independent  $\sigma_{ij}$  and  $\epsilon_{ij}$  to 6 (Love, 1927: 39, 79), and the number of independent  $c_{ijkl}$  to 36. The path independence of the energy required to strain a material reduce the number of independent  $c_{ijkl}$  to 21 (Love, 1927: 99). This last result implies  $c_{ijkl} = c_{klij}$ .

In contracted notation

$$\text{for } ij \text{ (or } kl\text{): } 11 \rightarrow 1, 22 \rightarrow 2, 33 \rightarrow 3, 23/23 \rightarrow 4, 13/31 \rightarrow 5, 12/21 \rightarrow 6 \quad (2)$$

the stress-strain law is (with  $c_{ijkl} \rightarrow C_{mn}$ )

$$\begin{bmatrix} \sigma_1 \\ \sigma_2 \\ \sigma_3 \\ \sigma_4 \\ \sigma_5 \\ \sigma_6 \end{bmatrix} = \begin{bmatrix} C_{11} & C_{12} & C_{13} & C_{14} & C_{15} & C_{16} \\ & C_{22} & C_{23} & C_{24} & C_{25} & C_{26} \\ & & C_{33} & C_{34} & C_{35} & C_{36} \\ & & & C_{44} & C_{45} & C_{46} \\ & & & & C_{55} & C_{56} \\ & & & & & C_{66} \end{bmatrix} \begin{bmatrix} \epsilon_1 \\ \epsilon_2 \\ \epsilon_3 \\ \epsilon_4 \\ \epsilon_5 \\ \epsilon_6 \end{bmatrix} \quad (3)$$

where the lower left triangular portion of the matrix  $C$  has been left blank to indicate the symmetry of  $C_{mn}$ . If, after a reflection about the plane  $x_1 = 0$ ,  $x_2 = 0$  ( $x_1$  and  $x_2$  are lateral coordinates, and  $x_3$  is vertical), the elastic constants are unchanged, the number of independent constants is reduced to 13 (Appendix A), i.e.  $C_{35} = C_{36} = C_{45} = C_{46} = C_{15} = C_{25} = C_{16} = C_{26} = 0$ . The stress-strain law, equation (3), reduces to

$$\begin{bmatrix} \sigma_1 \\ \sigma_2 \\ \sigma_3 \\ \sigma_4 \\ \sigma_5 \\ \sigma_6 \end{bmatrix} = \begin{bmatrix} C_{11} & C_{12} & C_{13} & C_{14} & & \\ & C_{22} & C_{23} & C_{24} & & \\ & & C_{33} & C_{34} & & \\ & & & C_{44} & & \\ & & & & C_{55} & C_{56} \\ & & & & & C_{66} \end{bmatrix} \begin{bmatrix} \epsilon_1 \\ \epsilon_2 \\ \epsilon_3 \\ \epsilon_4 \\ \epsilon_5 \\ \epsilon_6 \end{bmatrix} \quad (4)$$

and the material is referred to as monoclinic, with the  $x_3$ -axis contained by the symmetry plane. (Zero elements in the upper right of the triangle are left blank.) The normal to the symmetry plane can be thought of as making an angle  $\theta = 0$  with the  $x_1$ -axis. Surprisingly, if the normal to a second symmetry plane makes an angle  $\theta = \pi/c$  with the  $x$ -axis, where  $c$  is an irrational number, the material is symmetric for all  $\theta$  (Appendix B). Further, as shown by Love (1927: 152-155), the material has only 5 independent elastic constants (transverse isotropy). The stress-strain law for a TI medium is

$$\begin{bmatrix} \sigma_1 \\ \sigma_2 \\ \sigma_3 \\ \sigma_4 \\ \sigma_5 \\ \sigma_6 \end{bmatrix} = \begin{bmatrix} C_{11} & C_{12} & C_{13} & & & \\ & C_{11} & C_{13} & & & \\ & & C_{33} & & & \\ & & & C_{44} & & \\ & & & & C_{44} & \\ & & & & & C_{66} \end{bmatrix} \begin{bmatrix} \epsilon_1 \\ \epsilon_2 \\ \epsilon_3 \\ \epsilon_4 \\ \epsilon_5 \\ \epsilon_6 \end{bmatrix}, \quad (5)$$

where  $C_{66} = \frac{1}{2}(C_{11} - C_{12})$ .

The equation of motion can be developed (Appendix C) by equating the stress gradient with the product of density and particle acceleration (Love, 1927: 84-85)

$$\rho \frac{\partial^2 u_i}{\partial t^2} = \frac{\partial}{\partial x_j} \sigma_{ij} \quad (6)$$

or replacing  $\sigma_{ij}$

$$\rho \frac{\partial^2 u_i}{\partial t^2} = \frac{\partial}{\partial x_j} c_{ijkl} \frac{\partial u_k}{\partial x_l} \quad (7)$$

where  $u_i$  are components of displacement in the subscripted directions,  $\rho$  is the density of the material, and  $t$  is time, and  $\epsilon_{kl} = \partial u_k / \partial x_l$  is used. A plane wave solution to the wave equation may be written as (Daley and Hron, 1977)

$$u_i = U_i \exp(i\omega[t - \tau]) \quad (8)$$

where  $U_i$  are amplitude components,  $\omega$  is temporal frequency, and phase function  $\tau$  describes the travel time of the wavefront,

$$\tau = \omega[\mathbf{x} \cdot \mathbf{k}] \quad (9)$$

where the spatial coordinates are  $\mathbf{x} = (x_1, x_2, x_3)$ , the wavenumbers are  $\mathbf{k} = (k_1, k_2, k_3)$  and  $t =$  time. Substitution of the planewave (equation (8)) into the elastic-wave equation (7) gives

$$[\Gamma_{jk} - \lambda \delta_{jk}] U_j = 0 \quad (10)$$

where

$$\Gamma_{jk} = \frac{c_{ijkl}}{\rho} \frac{\partial \tau}{\partial x_l} \frac{\partial \tau}{\partial x_i} = \frac{c_{ijkl}}{\rho} p_i p_l, \quad (12)$$

and, assuming that  $U_i$  are not identically zero, the following eigenvalue problem results

$$\det[\Gamma_{jk} - \lambda \delta_{jk}] U_j = 0 \quad (11)$$

The components of slowness  $\mathbf{p} = (p_1, p_2, p_3)$  are

$$\begin{aligned} \frac{\partial \tau}{\partial x_1} &= \frac{\cos \psi \sin \theta}{v(\psi, \theta)} \\ \frac{\partial \tau}{\partial x_2} &= \frac{\sin \psi \sin \theta}{v(\psi, \theta)}, \\ \frac{\partial \tau}{\partial x_3} &= \frac{\cos \theta}{v(\psi, \theta)} \end{aligned} \quad (13)$$

with angle  $\theta$  measured from the  $x_3$  axis and azimuth  $\psi$  as in Figure 1. Velocity  $v(\psi, \theta)$  is the phase velocity of the wave type being considered.

Unfortunately, the determinant in equation (11) results in 6<sup>th</sup> order powers of  $v(\psi, \theta)$ , and a correspondingly unwieldy description. The solution is greatly simplified (Appendix D) when wave propagation in the  $y$  coordinate is ignored i.e.,  $\psi = 0$ . Three positive values of  $v$  result corresponding to quasi-P, quasi-SV and quasi-SH wavefront propagation (Daley and Hron, 1977). The equation for P-waves is

$$2\rho v_p^2 = C_{33} + C_{44} + (C_{11} - C_{33}) \sin^2 \theta + \sqrt{(C_{33} - C_{44})^2 + 2C_1 \sin^2 \theta + C_2 \sin^4 \theta} \quad (14)$$

where,

$$C_1 = 2[C_{13} + C_{44}]^2 - [C_{33} - C_{44}][C_{11} + C_{33} - 2C_{44}] \quad (15)$$

and

$$C_2 = [C_{11} + C_{33} - 2C_{44}]^2 - 4[C_{13} + C_{44}]^2 \quad (16)$$

P-wave velocity in a TI medium is thus a function of 4 of the 5 independent elastic constants and phase angle  $\theta$ . Thomsen (1986) presents a convenient rendering of P-wave velocity (as well as the qSV and qSH) in terms of parameters  $\alpha_0$ ,  $\beta_0$ ,  $\epsilon$  and  $\delta^*$ . The first two correspond to P-wave ( $\alpha_0$ ) and S-wave ( $\beta_0$ ) velocity measured parallel to the axis of TI symmetry. These four parameters are the following functions of the 4 elastic constants in equation (5)

$$\alpha_0 = \sqrt{\frac{C_{33}}{\rho}}, \beta_0 = \sqrt{\frac{C_{44}}{\rho}}, \quad (17)$$

and,

$$\varepsilon = \frac{C_{11} - C_{33}}{2C_{33}}, \delta^* = \frac{1}{2C_{33}^2} [2(C_{13} + C_{44})^2 - (C_{33} - C_{44})(C_{11} + C_{33} - 2C_{44})] \quad (18)$$

The exact P-wave phase velocity in terms of the Thomsen (1986) parameters becomes

$$v_p^2 = \alpha_0^2 [1 + \varepsilon \sin^2(\theta) + D^*(\theta)] \quad (19)$$

where,

$$D^*(\theta) = \frac{1}{2} [1 - \beta_0^2 / \alpha_0^2] \left[ -1 + \sqrt{1 + \frac{4\delta^*}{(1 - \beta_0^2 / \alpha_0^2)^2} \sin^2(\theta) \cos^2(\theta) + \frac{4\varepsilon(1 - \beta_0^2 / \alpha_0^2 + \varepsilon)}{(1 - \beta_0^2 / \alpha_0^2)^2} \sin^4(\theta)} \right] \quad (20)$$

In the next section, the equation (19) for P-wave phase velocity  $v_p$ , as a function of phase angle  $\theta$ , is related to the coordinates of Fourier space for the propagation of wavefields.

### STATIONARY PHASE SHIFT FOR TI MEDIA

Depth imaging in a homogeneous TI medium (the anisotropy is stationary in the lateral coordinates) is simple to develop from the stationary phase shift method of Gazdag (1978). In Gazdag's (1978) method, the spectrum of the recorded seismic wavefield is recursively extrapolated downwards. At each depth level, as the wavefield moves down, an imaging condition is invoked that forms the output data. Generalization of this method from an isotropic to anisotropic media exploits the relationship of horizontal slowness to wavenumber ( $k_x$ ) and temporal frequency ( $\omega$ ).

The phase shift extrapolator central to the Gazdag (1978) method is

$$\psi(x, z) = \frac{1}{2\pi} \int_{-\infty}^{\infty} \alpha(k_x) \phi(k_x, 0) \exp(-ixk_x) dk_x \quad (21)$$

where the monochromatic (in temporal frequency  $\omega$ ) wavefield  $\psi(z)$  is deduced from the  $k_x$  spectrum of  $\phi(z = 0)$ . Equation (21) carries spectrum  $\phi$  to space coordinates as a product with *symbol*  $\alpha$ . Symbol  $\alpha$  is given by

$$\alpha(k_x) = \exp\left(iz\sqrt{\left(\frac{\omega}{v}\right)^2 - k_x^2}\right). \quad (22)$$

Here, extrapolation is in the positive  $z$  direction, and  $v$  is the velocity in the medium.

The velocity  $v$  in equation (22) is held constant in all lateral coordinates and variation of  $v$  with depth is enabled by recursive extrapolation. Thus, the medium must be homogeneous and isotropic in the lateral coordinate. The demand for isotropy can be relaxed, however, because the phase shift method does not restrict velocity to constant wavenumbers.

Similar to the method of Kitchenside (1992), we exploit the relationship of horizontal slowness to wavenumber and frequency

$$p = \frac{\sin(\theta)}{v(\theta)} = \frac{k_x}{\omega}, \quad (23)$$

where  $v(\theta)$  is computed using equation (19). If the TI medium is dipping (i.e., the axis of TI symmetry is not vertical) equation (23) must be rotated by the angle between the axis of TI symmetry and vertical. In Figure 2 horizontal slowness  $p$  for Weathered Gypsum is plotted against phase angle  $\theta$ . A polynomial fit to this curve provides an empirical relationship between  $\theta$  and  $p$

$$\theta = a_0 + a_1 \frac{k_x}{\omega} + a_2 \left(\frac{k_x}{\omega}\right)^2 + \dots + a_n \left(\frac{k_x}{\omega}\right)^n, \quad (24)$$

where  $a_i$  are the polynomial coefficients. (The appropriate value for  $n$  is determined by numerical experimentation.) At every  $(k_x, \omega)$  in  $\varphi(0)$  a phase angle  $\theta$  is defined by equation (23) through the polynomial of equation (24), and the appropriate velocity is computed using equation (19). The phase shift symbol becomes

$$\alpha(k_x) = \exp\left(iz\sqrt{\left(\frac{\omega}{v(k_x/\omega)}\right)^2 - k_x^2}\right), \quad (25)$$

where  $v$  is now no longer constant but a function of horizontal slowness  $k_x/\omega$ .

A difficulty presents itself when the axis of symmetry  $\phi$  of the medium is nonzero (Tsvankin, 1997), as can be seen in Figure 2. A range of  $k_x/\omega$ , between the horizontal lines propagate only in the downward direction, but a smaller range between the horizontal lines on Figure 3 propagate simultaneously up and down. (The dashed part of the line indicates the upgoing part.) In a procedure similar to the turning wave migration of Hale et al. (1992) we separate the purely downgoing phases, corresponding to the solid line in Figure 2, from the upgoing phases and propagate them down. The upgoing phases, corresponding to the phases below the line on Figure 3, are then separated and propagated upward. However, only those phases corresponding to the dashed part of the curve are upgoing. Error is introduced in the

upgoing phases because phases corresponding to the solid part of the curve are also propagated upward. They should only be propagated down.

Figure 4 shows the depth-migration impulse-response of phase shift in a homogeneous TI medium. The axis of symmetry is 45 degrees. The material simulated is the Weathered Gypsum described by Thomsen (1986) the elastic parameters are annotated. The solid line represents a wavefront, or a line of constant time, computed by raytracing using group velocity (which is the velocity at which the wavefront propagates. Thomsen (1986) provides a formula for the derivation of this velocity from phase velocity. This theoretical curve is only kinematically correct. The migration impulse response tracks the theoretical curve very well. On the left side, the impulse response exceeds 90 degrees, but the migration impulse response is able to track it (distortion beyond 90° is due to the unavoidable up propagation of downgoing phases). The quality of the impulse response means that reliable imaging of structures, at least up to 90 degrees, is possible for a homogeneous TI medium. This is generalized to heterogeneous TI media in a later section.

### **Isotropic reef with an anisotropic overburden**

As a test of the homogeneous TI method, seismic data from a physical model, designed to simulate reef, were obtained from the Physical Modeling Facility at the University of Calgary, courtesy of the Foothills Research Project. The physical model consists of a block of Phenolic material with orthorhombic anisotropy overlying a block of Plexiglas that is isotropic. The overburden was oriented such that it responded to a 2-D acquisition as a TI medium. A step cut into the Plexiglas represents an imaging target such as a reef edge. Figure 5 shows the geometry of the model scaled into units of meters. The anisotropic parameters are labeled in Figure 5.

The resulting constant offset seismic data scaled into units of seconds and meters is shown in Figure 6. The offset between the source and receiver transducers is 200m in the scaled units. Imaging the constant offset data by TI phase shift provides an accurate picture of the model, as in Figure 7, where the imaged reef tracks the true reef, given by a dashed line, and the top of the isotropic material is correctly located. Figures 8 and 9 are included to illustrate the error of using an isotropic imaging method (Figure 8) or an imaging method that assumes a vertical axis of TI symmetry (VTI) (Figure 9) for a dipping TI medium. In both figures, reflectors are imaged approximately 60m to shallow and the reef edge is positioned approximately 400m to the left of the true position. The only difference between the isotropic and VTI images is found in their diffraction responses (at the top and bottom edges of the reef). The response corresponding to the VTI method is less steep than the isotropic method.

## **SYMMETRIC NONSTATIONARY PHASE SHIFT FOR TI MEDIA**

Symmetric nonstationary phase shift (Margrave and Ferguson, 1999b) uses nonstationary filter theory (Margrave, 1998) to remove the requirement that velocity remain constant in the lateral coordinate. The resulting symmetric operator is more accurate and more stable than other explicit wavefield extrapolators (Margrave and

Ferguson, 1999b). Phase shift, equation (21), written as a symmetric nonstationary filter operation is

$$\Psi(x, z) = \int_{-\infty}^{\infty} \Psi(y, 0) \frac{1}{2\pi} \int_{-\infty}^{\infty} \alpha\left(x, k_x, \frac{z}{2}\right) \alpha\left(y, k_x, \frac{z}{2}\right) \exp(-ik_x[x - y]) dk_x dy, \quad (26)$$

where the product of symbols  $\alpha(x)$  and  $\alpha(y)$  is

$$\alpha\left(x, k_x, \frac{z}{2}\right) \alpha\left(y, k_x, \frac{z}{2}\right) = \exp\left(\frac{iz}{2} \sqrt{\left(\frac{\omega}{v(x)}\right)^2 - k_x^2} + \frac{iz}{2} \sqrt{\left(\frac{\omega}{v(y)}\right)^2 - k_x^2}\right). \quad (27)$$

Lateral coordinates at  $z = 0$  (input) are represented by  $y$ , and output coordinates at  $z = 0$  are represented by  $x$ . (The equivalent linear operator in equation (26) is symmetric under an exchange of coordinates  $x$  and  $y$ .) Using the same polynomial fitting procedure as in the homogeneous TI case, except that a polynomial is created at every  $x$  and  $y$  location, the product of symbols  $\alpha(x)$  and  $\alpha(y)$  (equation (27)) for heterogeneous TI is

$$\alpha\left(x, k_x, \frac{z}{2}\right) \alpha\left(y, k_x, \frac{z}{2}\right) = \exp\left(\frac{iz}{2} \sqrt{\left(\frac{\omega}{v(x, \omega/k_x)}\right)^2 - k_x^2} + \frac{iz}{2} \sqrt{\left(\frac{\omega}{v(y, \omega/k_x)}\right)^2 - k_x^2}\right). \quad (28)$$

Ferguson and Margrave (1999) provide an efficient implementation of equation (28) for isotropic media. They break the symmetric extrapolator into two steps, and each step proceeds as a set of stationary phase shifts corresponding to a velocity profile that is piecewise continuous laterally. The extension to TI simply requires replacement of their isotropic extrapolator with the anisotropic one of equation (25). Then, instead of just P-wave velocity, all four anisotropic parameters are made piecewise continuous laterally.

Figures 12 and 14 are impulse responses for poststack migration by symmetric nonstationary phase shift for two different geological scenarios. Figure 12 is the impulse response for poststack migration through the velocity structure of Figure 11. The input to the experiment is given in Figure 10. The velocity structure of Figure 11 has Weathered Gypsum on the left side (with a 45 degree axis of symmetry), and a similar but isotropic material on the right. Figure 12 clearly shows the difference between wave propagation through an isotropic versus and anisotropic medium. The TI impulse response is skewed down and to the right while the isotropic curve is symmetric. In Figure 14, the impulse on the left has first propagated through an isotropic medium to a depth of 400m where it entered a TI medium (Figure 13). The resulting impulse response is symmetric from 0 to 400m and non-symmetric from 400m to 800m. The reverse is true for the right side. The impulse began in a TI medium and entered and isotropic medium at 400m (Figure 13), and is then non-symmetric from 0 to 400m and symmetric from 400m to 800m.

## **Anisotropic thrust sheet in an isotropic background**

A second physical model is that of a flat reflector overlain by a TI thrust sheet embedded in an isotropic background. It represents a true anisotropic/nonstationary problem (the anisotropic parameters vary in the lateral coordinate). The thrust sheet is composed of four blocks (Figure 15) – each with a different axis of TI symmetry. The base of the model consists of a flat aluminum plate that provides a strong reflection.

A single source gather is given in Figure 16 and spans the first 4000 m of the model with the source location at 2040m. The major reflection at the bottom of the gather corresponds to a reflection from the aluminum plate. The apparent moveout of the reflection is continuous because its energy has propagated only through the isotropic material of the Plexiglas, and the block of TI material with the vertical axis of symmetry. In contrast, to the right of the source location, reflected energy has propagated through all three of the TI blocks that have nonvertical axes of TI symmetry, and the resulting apparent moveout on the reflection is discontinuous.

TI depth migration of the source gather (Figure 17), using SNPS, results in an image of the aluminum plate that is flat on both sides of the source. The lack of continuity below the source location is due to the 200m gap in the near offsets on the source gather (Figure 16). Isotropic depth migration resolves a poor image of the aluminum plate (Figure 18).

The image provided by assembling all of the TI migrated source gathers (Figure 19) provides a very good image of the reflector at the correct depth, and even the joints between the blocks are correctly positioned. Assembling all of the source gathers from isotropic migration into a single image provides a distorted picture (Figure 20). The joints between blocks have been imaged, but in the wrong places, and the aluminum plate has a large artifact anticline formed directly below the dipping TI blocks.

## **CONCLUSIONS**

A new depth imaging method for dipping TI media was presented based on the symmetric nonstationary phase shift (SNPS) method of Ferguson and Margrave (1999). Their method is a cascade of two nonstationary extrapolators and is more accurate and more stable than other explicit-one-way extrapolators (Margrave and Ferguson, 1999b). It was adapted for depth imaging in a TI medium. No restriction was placed on the strength of the anisotropy, its heterogeneity or its axis of symmetry. Depth imaging of two TI models (physical seismic data) by SNPS provided superior images to those from isotropic and VTI (vertical transverse isotropy) methods.

## **ACKNOWLEDGEMENTS**

For providing the raw data presented above, we are grateful to Don Lawton and Helen Isaac of the Foothills Research Project (FRP), and Eric Gallant of the Consortium for Research in Elastic Wave Exploration Seismology (CREWES), all of the University of Calgary. For his technical assistance the authors thank Michael

Loughlean of Alberta Energy Company (AEC) Ltd. We also thank the sponsors of CREWES for their support of this research.

## REFERENCES

- Daley, P. F., and Hron, F., 1977, Reflection and transmission coefficients for transversely isotropic media: *Bull., Seis. Soc. Am.*, **67**, 661-675.
- Ferguson, R. J., and Margrave, G. F., 1999, Prestack depth migration by symmetric nonstationary phase shift: *Submitted to Geophysics*.
- Gazdag, J., 1978, Wave equation migration with the phase shift method: *Geophysics*, **43**, 1342-1351.
- Gonzalez, A., Lynn, W., and Robinson, W. F., 1991, Prestack frequency-wavenumber (f-k) migration in transversely isotropic medium: 61<sup>st</sup> Ann. Internat. Mtg., Soc. Expl. Geophys., Expanded Abstracts, 1155-1157.
- Hale, D., Hill N. R., Stefani, J., 1992, Imaging salt with turning waves: *Geophysics*, **57**, 1453-1463.
- Isaac J. H., and Lawton, D. C., 1999, Image mispositioning due to dipping TI media: A physical seismic modeling study: *Geophysics*, **64**, 1230-1238.
- Kitchenside, P. W., 1992, 2-D anisotropic migration in the space-frequency domain: *Journal of seismic exploration*, **2**, 7-22.
- Love, A. E. H., 1927, *A treatise on the mathematical theory of elasticity*: Cambridge University Press, Cambridge.
- Margrave, G.F., 1998, Theory of nonstationary linear filtering in the Fourier domain with application to time-variant filtering: *Geophysics*, **63**, 244-259.
- Margrave G. F., and Ferguson, R. J., 1999a, Wavefield extrapolation by nonstationary phase shift: *Geophysics*, **64**, 1067-1078.
- Margrave G. F., and Ferguson, R. J., 1999b, Taylor series derivation of nonstationary wavefield extrapolators: *CREWES Research Report this issue*.
- Martin, D., Ehinger, A., and Rasolofosaon, P N. J., 1992, Some aspects of seismic modeling and imaging in anisotropic media using laser ultrasonics: 62<sup>nd</sup> Ann. Internat. Mtg., Soc. Expl. Geophys., Expanded Abstracts, 1373-1376.
- Meadows, M. A., and Abriel, W. L., 1994, 3-D phase-shift migration in transversely isotropic media: 64<sup>th</sup> Annual Internat. Mtg., Soc. Expl. Geophys., Expanded Abstracts, 1331-1348.
- Meadows, M. A., Coen, S., and Liu, G., 1987, F-K migration in elliptically anisotropic media: 57<sup>th</sup> Ann. Internat. Mtg., Soc. Expl. Geophys., Expanded Abstracts, 659-661.
- Morgan, T. R., 1983, *Foundations of wave theory for seismic exploration*: International Human Resources Development Corporation.
- Sena, A. G., Toksoz, M. N., 1993, Kirchhoff migration and velocity analysis for converted and nonconverted waves in anisotropic media: *Geophysics*, **58**, 265-276.
- Stolt, R., 1978, Migration by Fourier transform: *Geophysics*, **43**, pp. 23-48.
- Thomsen, L., 1986, Weak elastic anisotropy: *Geophysics*, **51**, 1954-1966.
- Ting, T. C. T., 1996, *Anisotropic elasticity*: Oxford University Press, New York, Oxford.
- Tsvankin, I., 1997, Moveout analysis for transversely isotropic media with a tilted symmetry axis: *Geophysical Prospecting*, **45**, 479-512.
- Uren, N. F., Gardner, G. H. F., and McDonald, J. A., 1990, The migrator's equation for anisotropic media: *Geophysics*, **55**, 1429-1434.
- Uzcategui, O., 1995, 2-D depth migration in transversely isotropic media using explicit operators: *Geophysics*, **60**, 1819-1829.

## APPENDIX A

This appendix is adapted from Ting (1996: 40-48) and Love (1927: 127). Define the stress vector  $T_i$  as

$$T_i = \sigma_{ij} n_j \quad (A1)$$

where  $n_i$  are the components of a unit vector in the direction of  $T$ . Transformation of  $T$  to a new coordinate system by the orthogonal transform  $\Omega$  is

$$\begin{aligned} T'_i &= \Omega_{ij} T_j \\ &= (\sigma_{ij} n_j)' = (c_{ijkl} \epsilon_{kl} n_j)' \\ &= c'_{ijkl} \epsilon'_{kl} n'_j \end{aligned} \quad (A2)$$

where the prime indicates transformation to the new coordinate system. The elastic stiffnesses  $c'$  in the transformed coordinate system are given by

$$c'_{ijkl} = \Omega_{ip} \Omega_{jq} \Omega_{kr} \Omega_{ls} c_{pqrs} \quad (A3)$$

When  $c' = c$  the material possesses symmetry with respect to  $\Omega$

$$c_{ijkl} = \Omega_{ip} \Omega_{jq} \Omega_{kr} \Omega_{ls} c_{pqrs} \quad (A4)$$

If  $\Omega$  is specified as a reflection across a plane containing the  $x_3$  axis

$$\Omega(\theta) = \begin{bmatrix} -\cos 2\theta & -\sin 2\theta & 0 \\ -\sin 2\theta & \cos 2\theta & 0 \\ 0 & 0 & 1 \end{bmatrix} \quad (A5)$$

where  $\theta$  is the angle that the plane makes with the  $x_1$  axis then, for  $\theta = 0$

$$\Omega(\theta) = \begin{bmatrix} -1 & 0 & 0 \\ 0 & 1 & 0 \\ 0 & 0 & 1 \end{bmatrix} \quad (A6)$$

and equation (A4) requires that  $c_{ijkl} = 0$  whenever one or three of  $ijkl$  equals 1. Thus,  $c_{1112} = c_{1113} = c_{1222} = c_{1223} = c_{1233} = c_{1322} = c_{1323} = c_{1333} = 0$ , or, in the contracted notation  $C_{35} = C_{36} = C_{45} = C_{46} = C_{15} = C_{25} = C_{16} = C_{26} = 0$ .

## APPENDIX B

This appendix is adapted from Ting (1996: 42). If a material has reflection symmetry about the plane  $x = 0$ , and about a second plane making an angle of  $\theta_0$  with the  $x$ -axis (the axis of symmetry is the  $z$ -axis), the material has an infinite number of symmetry angles if  $\theta_0$  is equal to an irrational number times  $\pi$ . For example, for symmetry planes  $\theta = 0$  and  $\theta = \theta_0$ , and a vector  $\mathbf{x} = (x_1, x_2, x_3)$

$$\begin{aligned} \mathbf{x}^* &= \Omega(0)\mathbf{x}\Omega(\theta_0) \\ &= \begin{bmatrix} x \cos 2\theta_0 - y \sin 2\theta_0 \\ x \sin 2\theta_0 + y \cos 2\theta_0 \\ z \end{bmatrix}, \end{aligned} \quad (\text{B1})$$

can be written as a single operator

$$\mathbf{x} = \Omega(-\theta_0)\mathbf{x} \quad (\text{B2})$$

and

$$\begin{aligned} \mathbf{x}^* &= \Omega(\theta_0)\mathbf{x}\Omega(0) \\ &= \begin{bmatrix} x \cos 2\theta_0 + y \sin 2\theta_0 \\ -x \sin 2\theta_0 + y \cos 2\theta_0 \\ z \end{bmatrix}, \end{aligned} \quad (\text{B3})$$

can be written as a single operator

$$\mathbf{x} = \Omega(2\theta_0)\mathbf{x} \quad (\text{B4})$$

Thus, if a material has symmetry planes at  $\theta = 0$  and  $\theta = \theta_0$  the material also has symmetry planes at  $-\theta_0$  and  $2\theta_0$ . In fact, by applying the process repeatedly, the material has symmetry planes at  $\theta = k\theta_0$  where  $k$  can be positive or negative. When  $\theta_0$  is a rational number times  $\pi$ , say,  $\pi/2, \pi/3, \pi/4, \dots, a\pi/b$ , where  $a$  and  $b$  are integers, then

$$k\theta = \dots, -\frac{a\pi}{b}, \frac{a\pi}{b}, 2\frac{a\pi}{b}, 3\frac{a\pi}{b}, \dots, a\pi, \dots, 2a\pi, \dots, 4a\pi, \dots \quad (\text{B5})$$

implies a finite number of angles of symmetry about  $z$ . For  $\theta_0$  that is an irrational number times  $\pi$  then

$$k\theta = \dots, -\frac{\pi}{c}, \frac{\pi}{c}, 2\frac{\pi}{c}, \dots \quad (\text{B6})$$

implies an infinite number of angles of symmetry. A material with infinitely many angles of symmetry about  $z$  is transversely isotropic.

### APPENDIX C

This appendix is adapted from Love (1927: 84-85) and Morgan (1983: 36-38). From Figure C-1, a single component of force is a function of strains  $\sigma_{ij}$

$$\begin{aligned}
 F_x &= \left( \sigma_{xx} + \frac{\partial \sigma_{xx}}{\partial x} \Delta x \right) \Delta y \Delta z - \sigma_{xx} \Delta y \Delta z + \left( \sigma_{xy} + \frac{\partial \sigma_{xy}}{\partial y} \Delta y \right) \Delta x \Delta z - \sigma_{xy} \Delta x \Delta z \\
 &+ \left( \sigma_{xz} + \frac{\partial \sigma_{xz}}{\partial z} \Delta z \right) \Delta x \Delta y - \sigma_{xz} \Delta x \Delta y \\
 &= \frac{\partial \sigma_{xx}}{\partial x} \Delta x \Delta y \Delta z + \frac{\partial \sigma_{xy}}{\partial y} \Delta x \Delta y \Delta z + \frac{\partial \sigma_{xz}}{\partial z} \Delta x \Delta y \Delta z
 \end{aligned} \tag{C1}$$

where  $\Delta x$ ,  $\Delta y$  and  $\Delta z$  are the lengths of the sides of a small volume of material. Then, for force  $F_i$

$$F_i = \frac{\partial \sigma_{ij}}{\partial x_j} \Delta x \Delta y \Delta z \tag{C2}$$

The force due to the applied stress is opposed by force due to the mass of the material displaced i.e.

$$F_i = \frac{\partial^2 u_i}{\partial t^2} \rho \Delta x \Delta y \Delta z \tag{C3}$$

where  $\rho$  is the density of the material and  $u_i = (u_1, u_2, u_3)$  are displacements in the coordinate directions. Equating (D2) and (D3) gives the equation of motion

$$\rho \frac{\partial^2 u_i}{\partial t^2} = \frac{\partial \sigma_{ij}}{\partial x_j}, \tag{C4}$$

and, applying the stress-strain law (equation (1))

$$\rho \frac{\partial^2 u_i}{\partial t^2} = \frac{\partial}{\partial x_j} [c_{ijkl} \epsilon_{kl}] \tag{C5}$$

The definition of strain, defined in terms of displacements  $u_i$  is

$$\epsilon_{kl} = \frac{1}{2} \left( \frac{\partial u_k}{\partial x_l} + \frac{\partial u_l}{\partial x_k} \right), \tag{C6}$$

and, upon replacement in the equation of motion (C5), and using  $c_{ijkl} = c_{ijlk}$  (Ting, 1996: 32)

$$\rho \frac{\partial^2 u_i}{\partial t^2} = \frac{\partial}{\partial x_j} \left[ c_{ijkl} \frac{\partial u_k}{\partial x_l} \right]. \tag{C7}$$

#### APPENDIX D

This appendix is adapted from Daley and Hron (1977). The determinant in equation (11) can be written

$$\det \begin{pmatrix} p_1^2 A_{11} + p_2^2 A_{66} + p_3^2 A_{44} - 1 & p_1 p_2 A_{66} & p_1 p_3 [A_{13} + A_{44}] \\ p_1 p_2 A_{66} & p_1^2 A_{66} + p_2^2 A_{22} + p_3^2 A_{44} - 1 & p_2 p_3 [A_{23} + A_{44}] \\ p_1 p_3 [A_{13} + A_{44}] & p_2 p_3 [A_{23} + A_{44}] & p_1^2 A_{44} + p_2^2 A_{44} + p_3^2 A_{33} - 1 \end{pmatrix} = 0 \quad (D1)$$

where  $A_{mn}$  is related to the  $C_{mn}$  and density  $\rho$  by

$$A_{mn} = \frac{C_{mn}}{\rho}, \quad (D2)$$

with  $A_{66} = \frac{1}{2\rho} [C_{11} - C_{12}]$ . The components of slowness are

$$\frac{\partial \tau}{\partial x_i} = p_i. \quad (D3)$$

Replacement of the slownesses  $p_i$  with their corresponding functions of velocity, equations (12) in the text, and solving the determinant, results in 6<sup>th</sup> order values for  $v$  and a very complicated relation.

For a 2D medium, the  $(x_1, x_3)$  plane with the azimuthal angle  $\phi = 0$ , equation (D1) becomes

$$\det \begin{pmatrix} p_1^2 A_{11} + p_3^2 A_{44} - 1 & 0 & p_1 p_3 [A_{13} + A_{44}] \\ 0 & p_1^2 A_{12}^{11} + p_3^2 A_{44} - 1 & 0 \\ p_1 p_3 [A_{13} + A_{44}] & 0 & p_1^2 A_{44} + p_3^2 A_{33} - 1 \end{pmatrix} = 0. \quad (D4)$$

The solution of equation (D4) is only third order in  $v$  implying 3 roots corresponding to 3 modes of wave propagation, quasi-P, quasi-SV and quasi-SH. The solution for P-wave velocity  $v_p$  is given by equation (13) in the text.

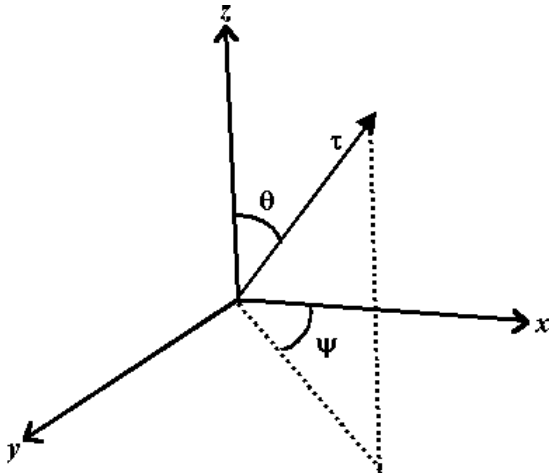


Fig. 1. Angle  $\theta$  is the inclination of travel time  $\tau$ , normal to a planewave, from the  $z$  axis. The  $z$  axis is aligned with the TI axis of symmetry. Angle  $\psi$  is angle relative to the  $x$  axis.

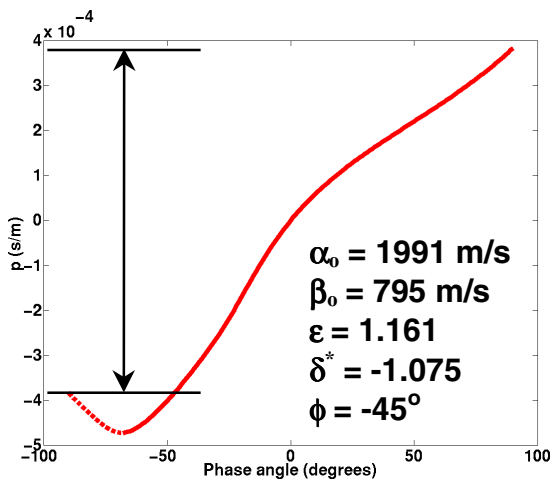


Fig. 2. Horizontal slowness  $p$  vs. phase angle  $\theta$  for Weathered Gypsum. (The anisotropic parameters are annotated.) This material was chosen due to its extreme anisotropy. The range of  $p = k_x/\omega$  between the solid lines are phases that are propagated down. The phases corresponding to the solid part of the curve out side of the lines are propagated simultaneously up and down. The down going phases are responsible for the coherent energy up to 90 degrees on Figure 4.

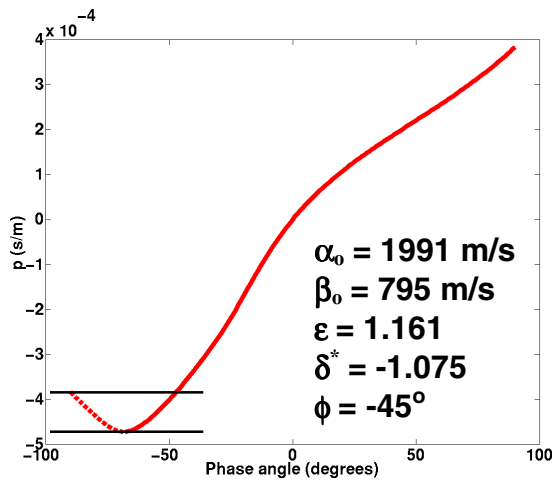


Fig. 3. Horizontal slowness  $p$  vs. phase angle  $\theta$  for Weathered Gypsum. The phases corresponding to the dashed line are propagated up, however they cannot be separated from the downgoing phases corresponding to the solid part of the curve between the lines. These phases are propagated up as well. The result in the impulse response of Figure 4 is the ability to track the theoretical response, though only approximately, beyond 90 degrees.

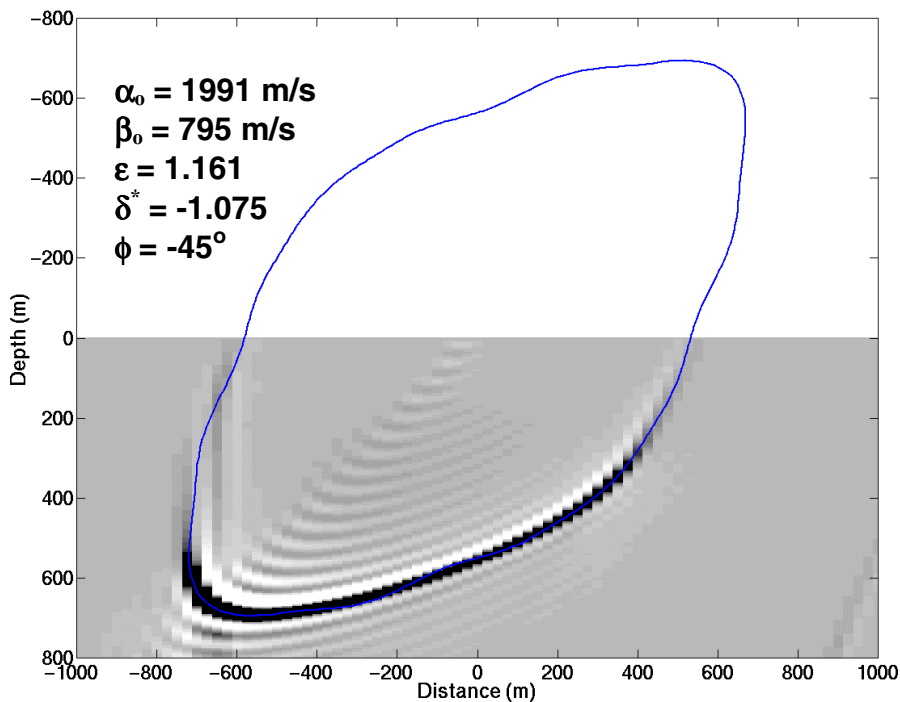


Fig. 4. The impulse response (equivalently a constant time curve) for phase shift in a homogeneous TI medium whose axis of symmetry is  $45^\circ$ . (This impulse corresponds to poststack depth imaging.) The continuous curve is the theoretical curve up to  $90^\circ$ . Beyond  $90^\circ$  the tracking is somewhat distorted due to the unavoidable propagation upwards of downgoing phases (see Figure 3).

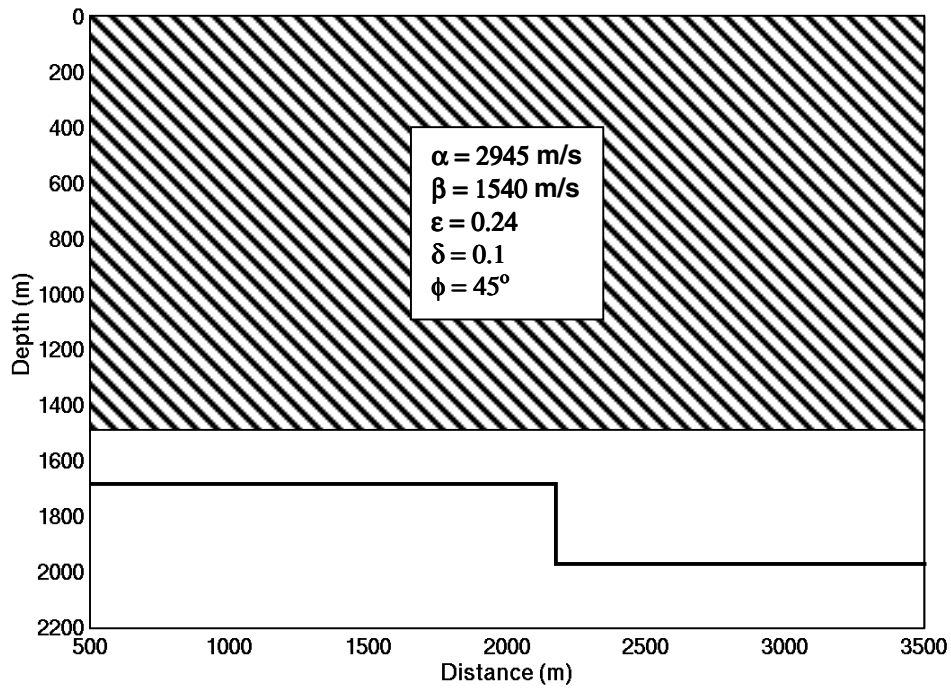


Fig. 5. Model of an isotropic reef with an anisotropic overburden. The dimensions and elastic parameters of the model are annotated. The axis of TI symmetry in the overburden is  $45^\circ$ .

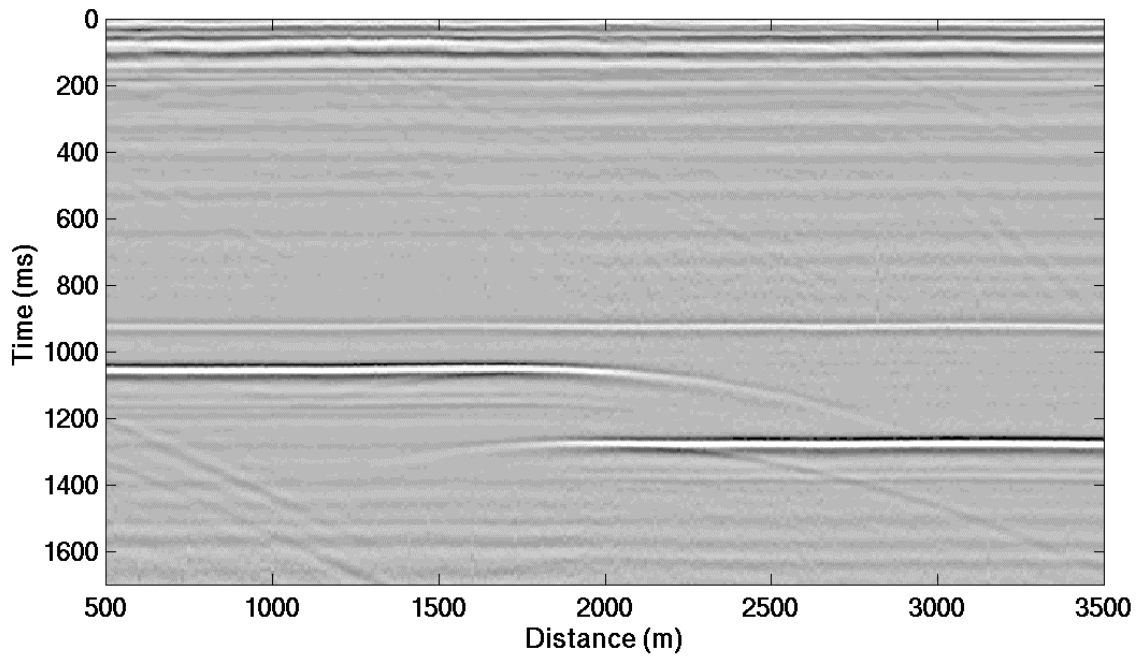


Fig. 6. Constant offset seismic data acquired from the model in Figure 5.

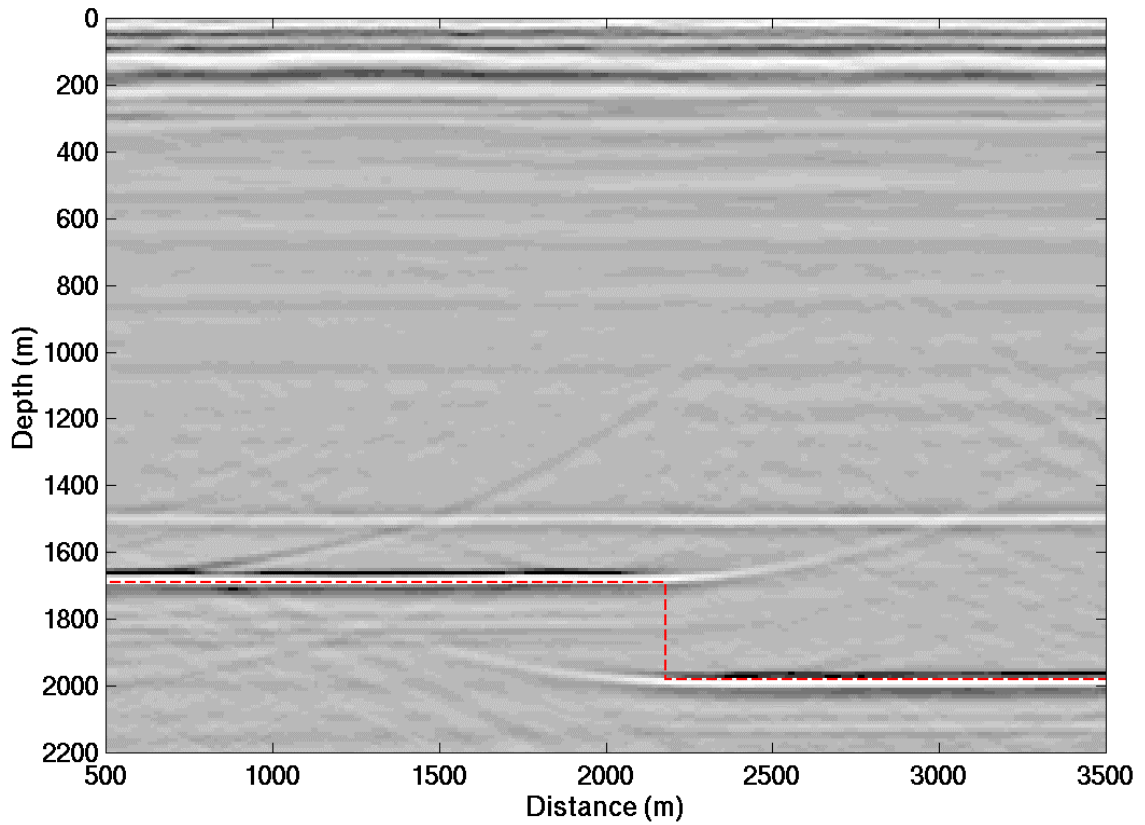


Fig. 7. Depth image of the constant offset data in Figure 6 using SNPS. The interface between the anisotropic overburden and the isotropic target zone is correctly positioned in depth (~ 1440m). The reef surfaces and reef edge have been correctly positioned in depth and lateral location (the true geometry of the reef is represented by the dashed line).

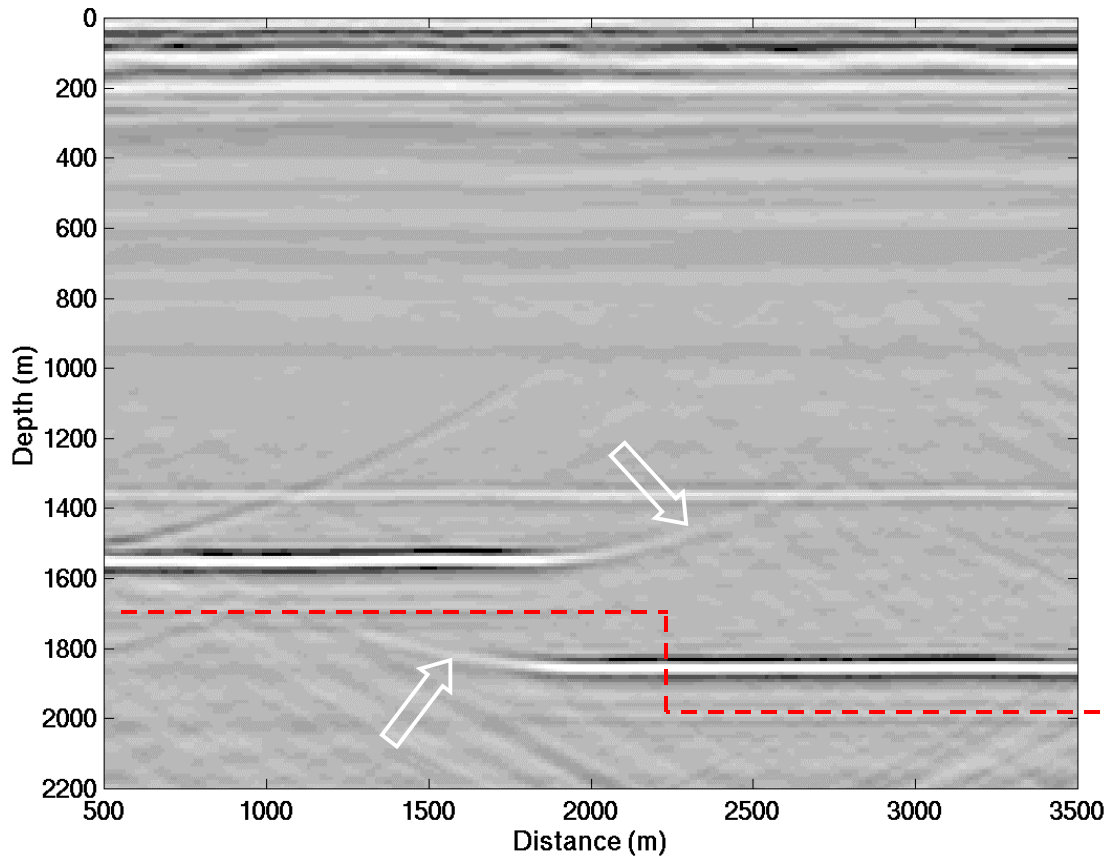


Fig. 8. Isotropic depth image of the constant offset data (Figure 6). Flat lying reflectors are positioned ~ 60m too shallow, and the reef edge is shifted ~ 400m to the left. Diffractions from the top and bottom of the reef edges are annotated for comparison with Figure 9.

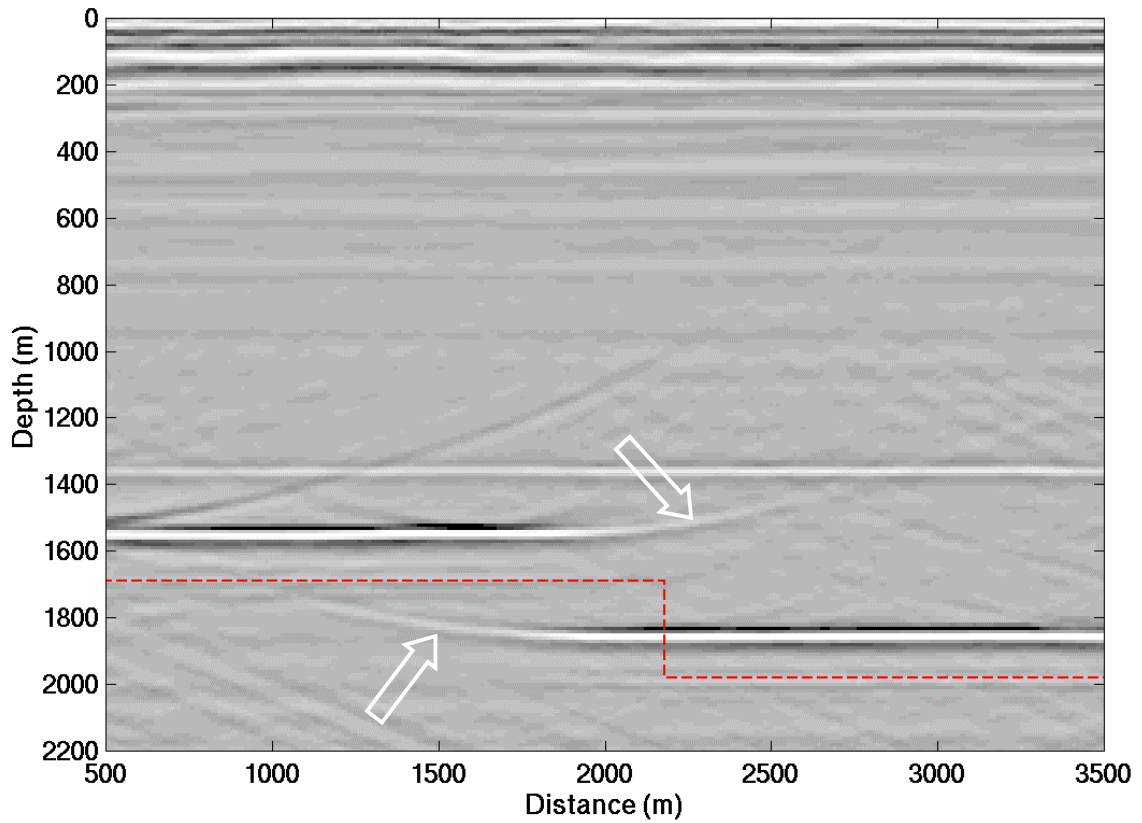


Fig. 9. Depth image of the constant offset data (Figure 6) assuming a vertical axis of TI symmetry (VTI). All flat lying reflectors are positioned  $\sim 60\text{m}$  too shallow in depth. The reef edge is positioned  $\sim 400\text{m}$  to the left of its true position. This image, and the isotropic image above (Figure 8), differ significantly in their diffraction responses as seen at the reef edges (arrows), but nowhere else.

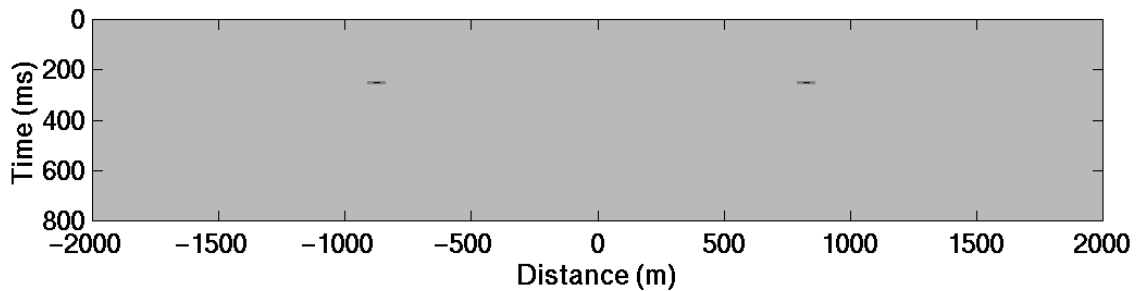


Fig. 10. Input impulses for depth imaging tests.

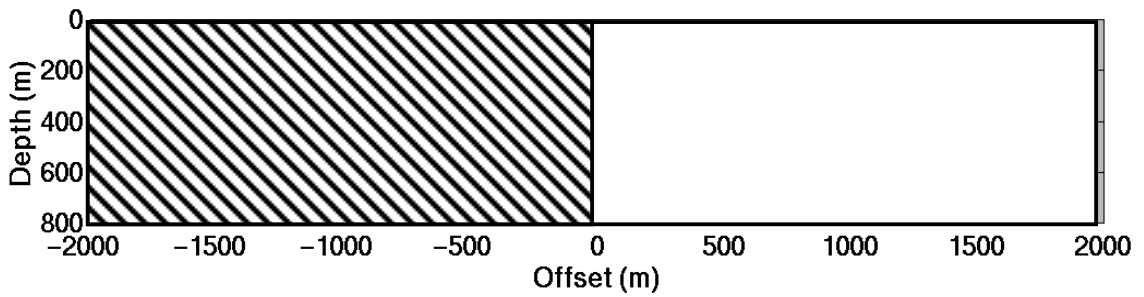


Fig. 11. Model of anisotropic Weathered Gypsum (see Figure 4 for the anisotropic parameters) welded laterally to isotropic Weathered Gypsum ( $\epsilon$  and  $\delta^+$  are zero). On the left, the axis of TI symmetry is  $45^\circ$ .

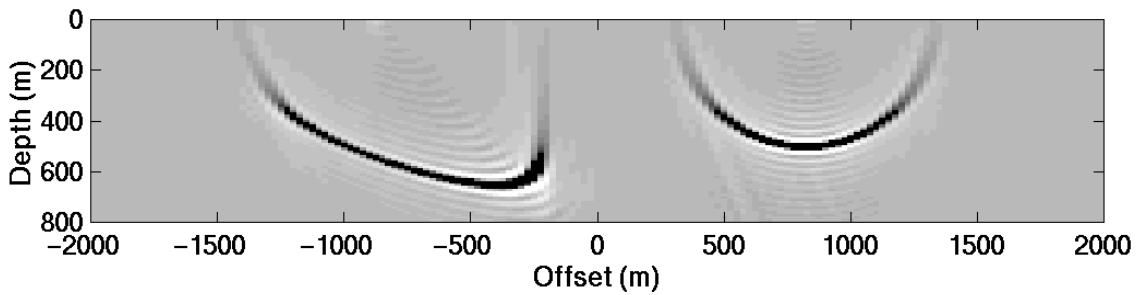


Fig. 12. Impulse response of SNPS for the model of Figure 11. The symmetry of the impulse response on the right side compared to the asymmetry of the left side demonstrates the ability of the method to migrate through heterogeneous TI media.

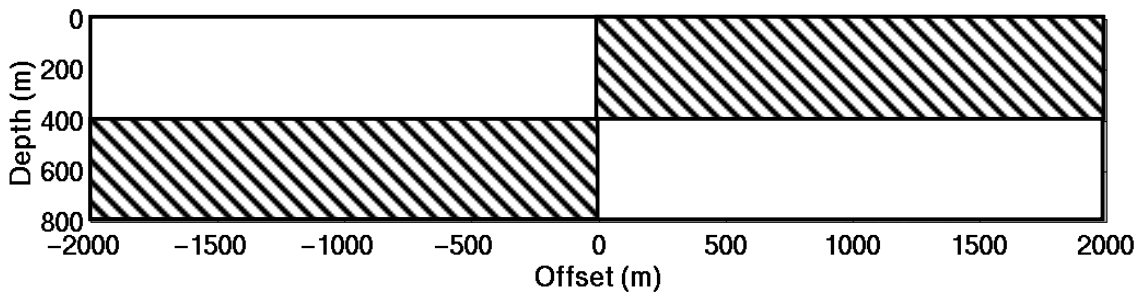


Fig. 13. Model of a heterogeneous TI medium where the quadrants of the model in Figure 11 have been swapped.

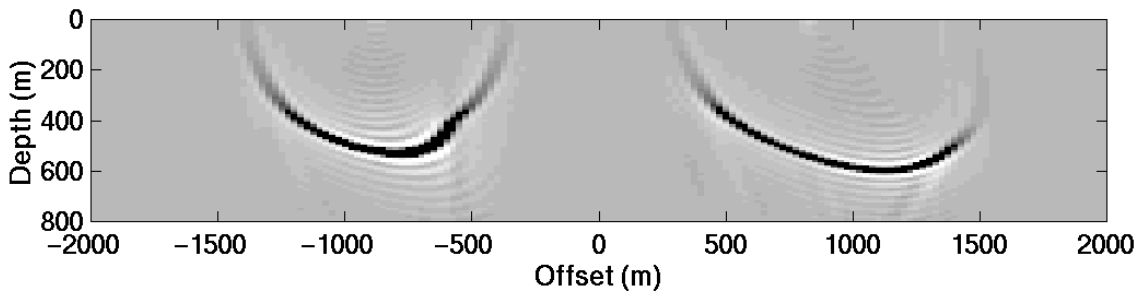


Fig. 14. Impulse response of SNPS for the model of Figure 13. The impulse response on the left side is symmetric until 400m where it encounters the dipping TI medium and becomes antisymmetric. The right side is anti symmetric until 400m where it encounters an isotropic medium and continues as a symmetric response.

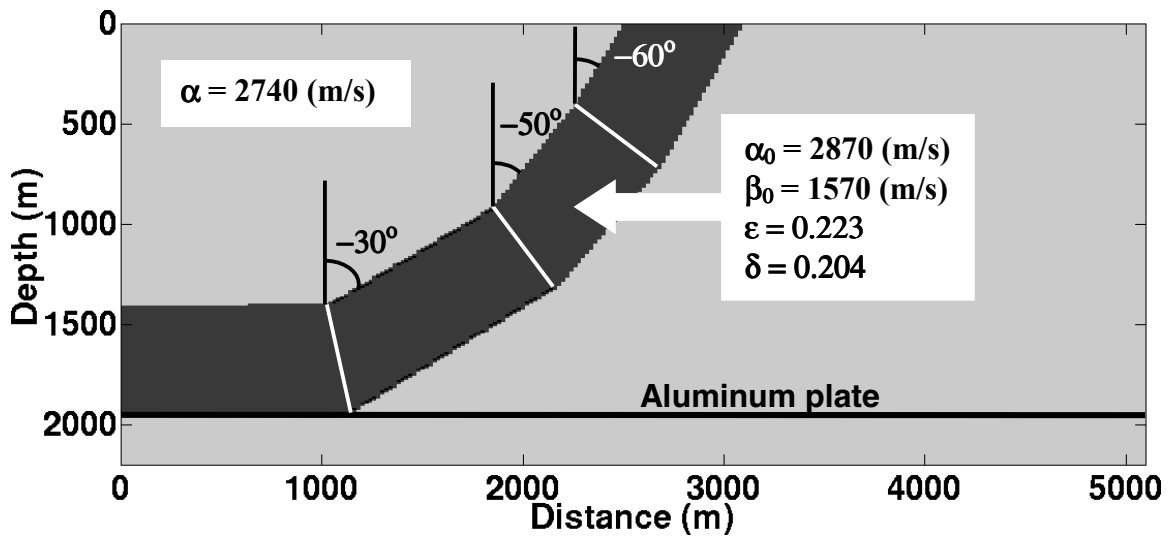


Fig. 15. Model of a TI thrust sheet embedded in an isotropic background. The thrust sheet is composed of four blocks of TI material with similar anisotropic parameters (annotated) but different axes of symmetry.

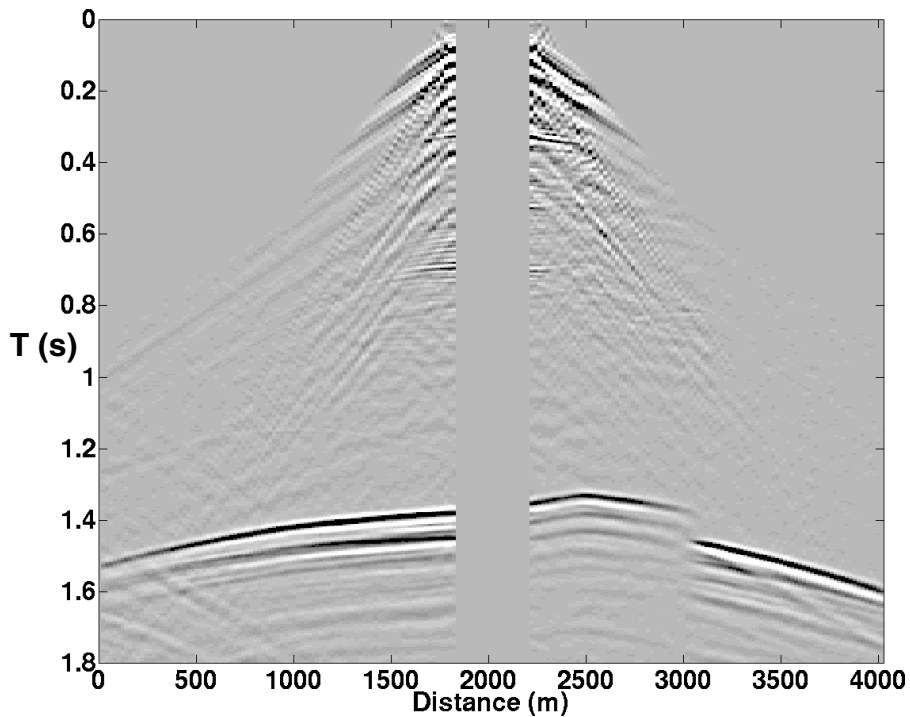


Fig. 16. Seismic source gather corresponding to source location 2040m in Figure (15). The major reflection at the bottom of the section corresponds to the base of the model. The apparent moveout of the reflection to the left of the source is continuous because most of the reflection energy propagated only through the isotropic material part of the model and the TI block with the vertical axis of symmetry. The reflection energy to the right of the source has propagated through the three blocks with nonvertical axes of TI symmetry and so appears discontinuous.

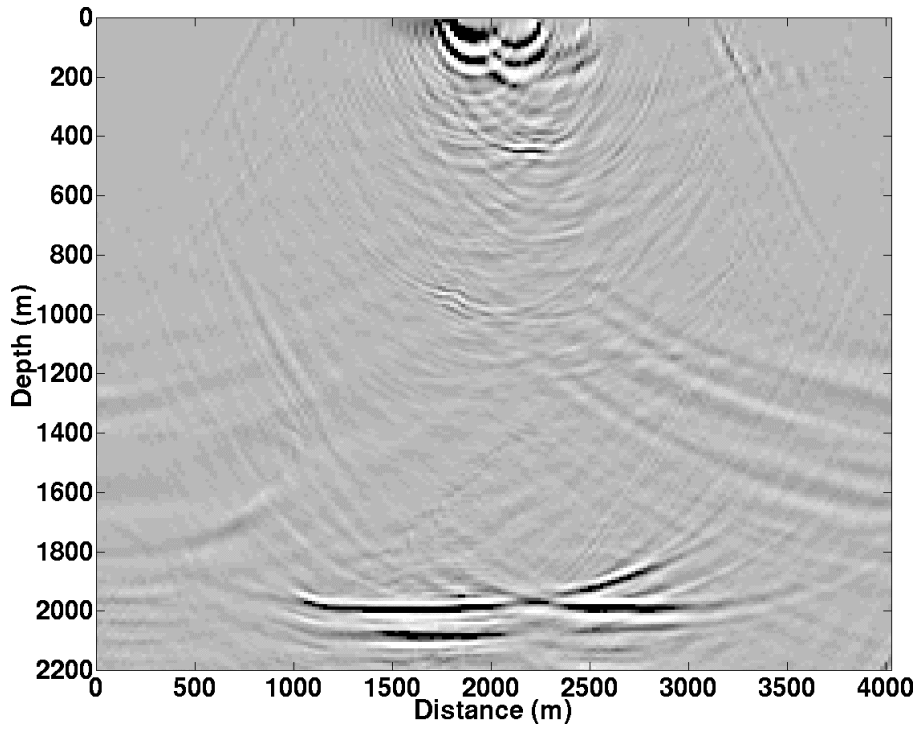


Fig. 17. TI depth migration of the source gather in Figure 16 by SNPS. The base of the model is correctly imaged. The discontinuity of the image below the show point corresponds to the gap between the live traces centered on the source location (Figure 16).

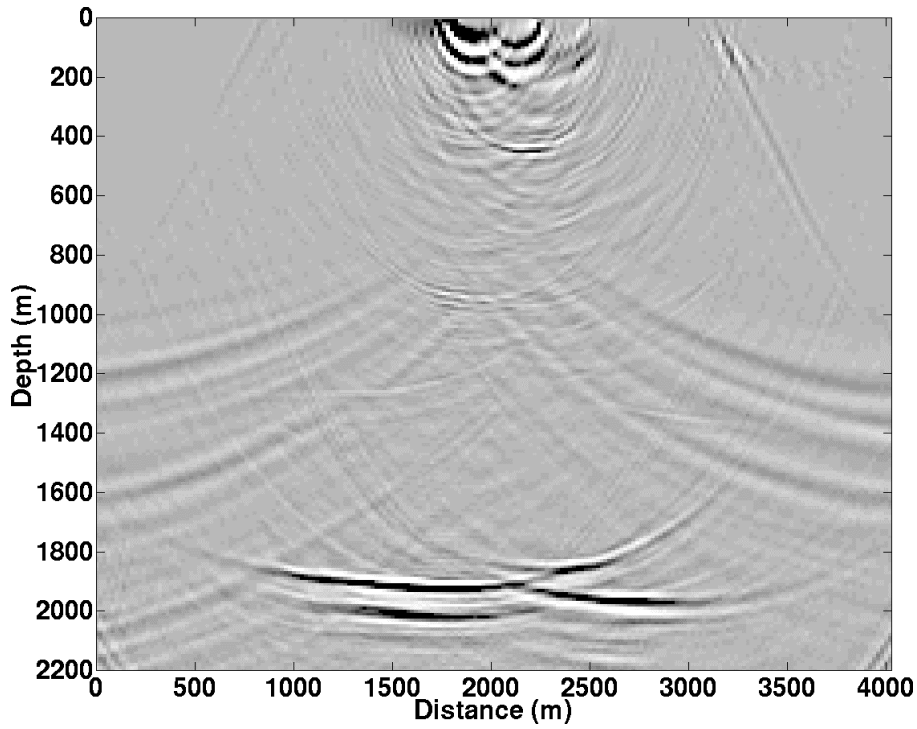


Fig. 18. Isotropic depth migration of the source gather in Figure 16. The base of the model has been poorly imaged demonstrating the need for TI migration.

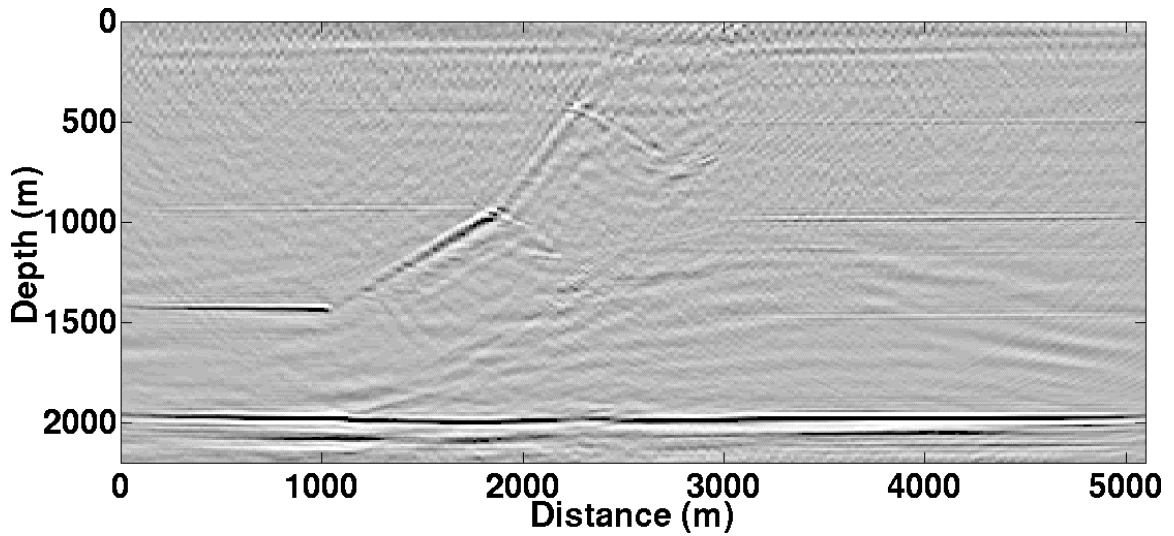


Fig. 19. The superposition of all SNPS-imaged source gathers. The base of the model has been correctly imaged, and the interfaces between the TI blocks are imaged and positioned quite well compared to the model (Figure 14) and the image from isotropic migration (Figure 18).

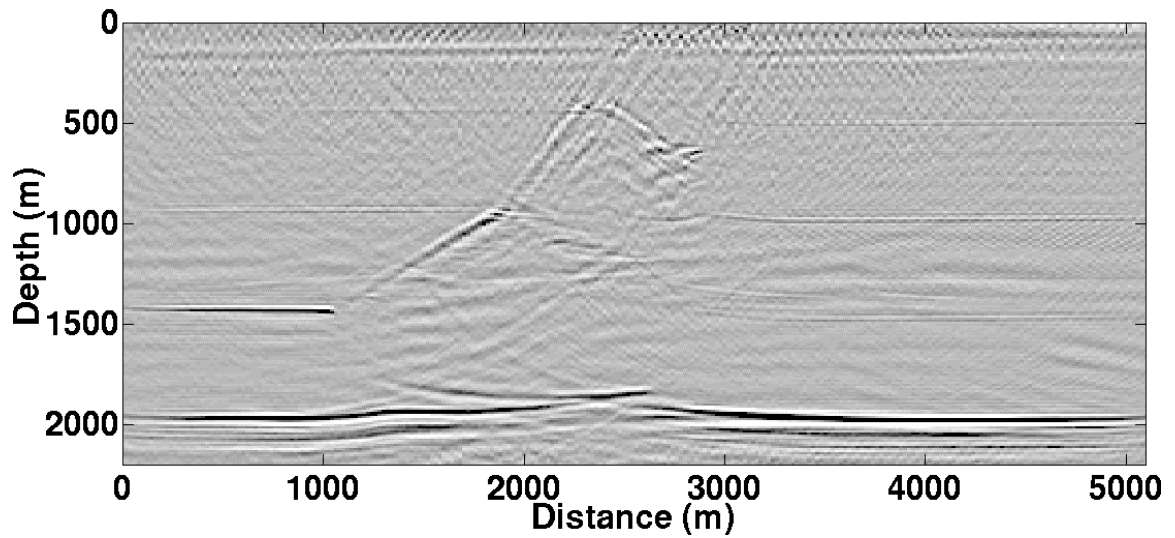


Fig. 20. The superposition of all isotropic-depth images of the source gathers. The base of the model has been poorly imaged, and the interfaces between the TI blocks are mispositioned.

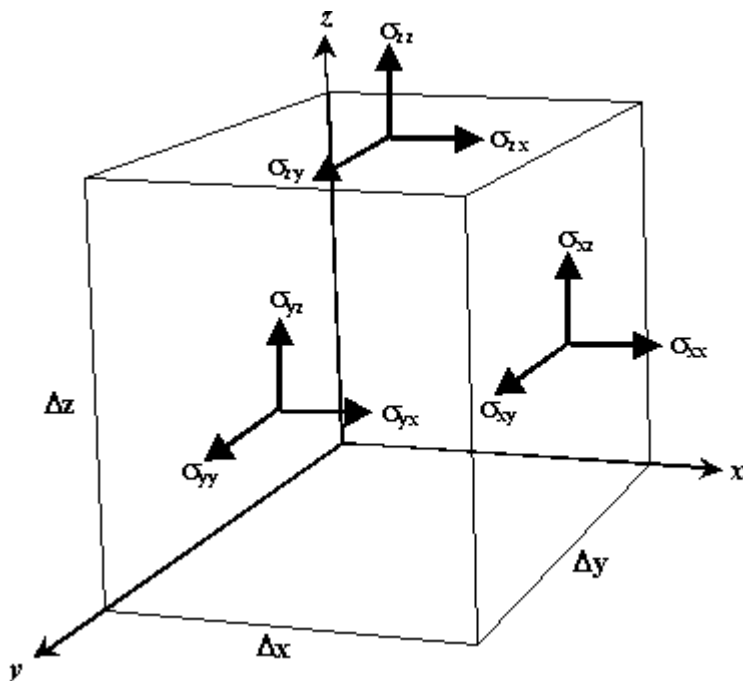


Fig. 21. Components of stress  $\sigma_j$  acting on a small volume whose sides are  $\Delta x$ ,  $\Delta y$  and  $\Delta z$ .